

Contents lists available at ScienceDirect

Journal of Energy Chemistry

JOURNAL OF ENERGY CHEMISTRY

http://www.journals.elsevier.com/

journal homepage: www.elsevier.com/locate/jechem

One-pot synthesis of FeNxC as efficient catalyst for high-performance zinc-air battery

Yang Li ^{a,b,1}, Kuanda Xu ^{a,1}, Qi Zhang ^b, Zhi Zheng ^b, Shunning Li ^a, Qinghe Zhao ^a, Can Li ^c, Cheng Dong ^a, Zongwei Mei ^{a,*}, Feng Pan ^{a,*}, Shixue Dou ^b

- ^a School of Advanced Materials, Peking University Shenzhen Graduate School, Shenzhen 518055, Guangdong, China
- b Institute for Superconducting and Electronic Materials, University of Wollongong, Wollongong, NSW 2522, Australia
- ^cCollege of Optical and Electronic Technology, China Jiliang University, Hangzhou 310018, Zhejiang, China

ARTICLE INFO

Article history: Received 10 February 2021 Revised 4 July 2021 Accepted 17 July 2021 Available online 29 July 2021

Keywords: FeNxC Oxygen reduction reaction Zinc-air battery

ABSTRACT

Rechargeable zinc-air batteries (ZAB) with a high theoretical energy density of 1086 Wh kg⁻¹, have received tremendous research attention. However, the practical application of ZABs is still limited by high polarization and poor energy efficiency (low power density) due to the sluggish 4 electrons (e⁻)/oxygen (O₂) kinetics over the air electrode. Here, a noble-metal-free FeNxC electrocatalyst is developed via a one-pot approach, which provides a high density of the oxygen reduction reaction (ORR) active site and facilitates the ORR kinetics. Accordingly, the as-assembled Zn-air battery displayed a low charge-discharge voltage gap of 0.71 V at 10 mA cm⁻², a remarkable peak power density as high as 181.2 mW cm⁻², as well as the long-term durability for hundreds of hours, among the top level of those reported previously. Our work provides a major boost for the practical application of Zn-air battery in the future.

© 2021 Science Press and Dalian Institute of Chemical Physics, Chinese Academy of Sciences. Published by ELSEVIER B.V. and Science Press. All rights reserved.

1. Introduction

Developing renewable energy conversion and storage system is promising for addressing the issues of global energy and environmental degradation [1–3]. Among various advanced technologies, metal-air battery, especially rechargeable zinc-air battery (ZAB) has been regarded as one of the most promising next-generation energy storage system due to its high theoretical energy densities, low-cost and high safety [3–7]. As the heart of Zn-air battery, the oxygen reduction reaction (ORR) plays an important role in determining the overall efficiency of ZAB [8–10]. Although precious metal-based electrocatalyst, like Pt/C, possesses fast ORR kinetics, high cost and poor durability of the noble-metal based catalyst have hampered the widespread commercialization of these energy conversion and storage technologies [11]. Therefore, it is highly desirable to rationally design noble-metal-free electrocatalysts towards efficient ORR for Zn-air battery.

Single atom catalysts (SACs) have emerged as a new research frontier in catalysis, due to the size effects on the geometric and electronic structures of metal species, the extremely high atom uti-

lization efficiency and large number of exposed active sites [12-17]. Among these SACs materials, M-N-C-based configuration (M, cost-effective transition metals) has been regarded as the most promising alternatives for noble metal. Numerous studies on Ndoped carbon SACs have been developed for ORR, such as Fe [18-21], Cu [9,22], Co [23,24], Zn [25], Cr [26], Ru [27], and Ir [28]. Among a variety of SACs, both theoretical and experimental results evidenced that Fe-N-C can provide the most favourable ORR kinetics [13,29-32]. Benefiting from its proper adsorption energy of reaction intermediates during ORR [29,33], which has been regarded as a viable alternative for the state-of-art Pt-based ORR catalyst [19,34-37]. Despite the advantages of Fe-N-C, its fabrication involves multi-step preparation and post-processing procedure which make it difficult to scale up to industrial level. Moreover, complicated process introduces metal oxide nanoparticle and some impurities, which may lower the atom utilization efficiency and reduce synthetic efficiency. To the best of our knowledge, the reports on the direct one-pot synthesis of SACs on the two-dimensional (2D) carbon layer have not been explored. Therefore, developing a cost-effective and convenient method for preparing high-quality FeNxC, is urgent need for large-scale application.

Herein, we develop a direct one-pot approach that can effectively synthesize high-purity FeNxC as superior ORR electrocata-

^{*} Corresponding authors.

E-mail addresses: meizw@pkusz.edu.cn (Z. Mei), panfeng@pkusz.edu.cn (F. Pan).

¹ These authors contributed equally to this work.

lyst. The resultant catalyst exhibited predominant ORR kinetics with excellent stability, which is even superior to the state-of-the-art Pt/C. As a result, the rechargeable ZAB with the FeNxC, which can deliver a large power density up to 181.2 mW cm⁻² and shrunken voltage gap of 0.71 V even at current density of 10 mA cm⁻² along with excellent stability. This work shines fresh light on fabricating highly efficient ORR catalysts for metal-air batteries, as well as provides a general method to synthesize SACs catalyst on 2D carbon layer.

2. Experimental

2.1. Materials

Glucose (GC), dicyandiamide (DCDA), FeCl₂ and FeCl₃ were purchased from Sigma-Aldrich. All reagents were of analytical grade and used directly without further treatment.

2.2. Synthesis of N-doped carbon (NC) and FeNxC

The synthetic procedure is illustrated in Fig. 1(a). NC was prepared via a two-step one-pot pyrolysis method, using GC and DCDA as carbon source and nitrogen source, respectively. Typically, the GC was mixed with DCDA (mass ration: 1:40), and the mixture was sintered under flowing Ar at 550 °C for 6 h to prepare the C₃N₄. Subsequently, the resulting product was carbonized at 900 °C for 3 h under Ar atmosphere. The process of preparing FeNxC is same as the NC, except for adding 4.53 mg FeCl₂ and 6.05 mg FeCl₃.

2.3. Materials characterization

The phase data were analyzed by X-ray powder diffraction (XRD) on an MMA diffractometer equipped with Cu K_{α} radiation (GBC, MMA), which operated from 10° to 80° in continuous scan mode with a scan rate of 2° min⁻¹. The structure and morphology of the sample were investigated on a field emission scanning electron microscope (FESEM; JEOL JSM-7500) and a transmission electron microscope (TEM; JEOL-2010). Atomic resolution analytical microscope investigations were conducted using scanning TEM (STEM; JEOL ARM 200F), which was operated at 80 keV and equipped with a cold field emission high-resolution pole piece and a Centurio energy dispersive spectroscopy (EDS) detector. X-ray photoelectron spectroscopy (XPS) experiments were carried out on a VG Scientific ESCALAB 2201XL instrument using aluminum K_{α} X-ray radiation.

2.4. Electrochemical measurements

All electrochemical tests were conducted on a PINE electrochemical instrumentation equipped with a high-speed rotator and three electrodes system. The Pt wire and Ag/AgCl were used as the counter and reference electrode, respectively. For preparing the working electrode, 2 mg of as-prepared catalyst or 20% Pt/C+lrO $_2$ (1:1) was dispersed into 1 mL isopropanol (with 1‰ Nafion solution) and sonicated for 2 h to form homogenous ink. Then, 30 μL of the catalyst dispersion (2 mg mL $^{-1}$) was transferred on the surface of glassy-carbon electrode of RDE (0.196 cm 2). The measured potential vs. Ag/AgCl was converted to the reversible hydrogen electrode (RHE) scale according to the following equation:

$$E(RHE) = E(Ag/AgCl) + 0.0591 \times pH + 0.197 V,$$

where $E_{Ag/AgCl}$ is the measured potential vs. the Ag/AgCl reference and $E_{Ag/AgCl}^0$ is 0.197 V. The pH values for 0.1 M KOH and 1 M KOH are 13 and 13.8, respectively.

The ORR performance was investigated by linear sweep voltam-mogram (LSV) measurements in O_2 -saturated 0.1 M KOH with scan rate of 10 mV s⁻¹ at rotation speed from 400 to 2050 r min⁻¹. The electron transfer number (n) per O_2 during the ORR process was calculated by the Koutechy-Levich equation:

$$\frac{1}{J} = \frac{1}{J_k} + \frac{1}{J_L} = \frac{1}{J_k} + \frac{1}{B\omega^{1/2}}$$

$$B = 0.62 nFC_0 D_0^{2/3} v^{-1/6}$$

where J is the response current density during ORR, J_k is the kinetic current density, ω is the electron rotating angular velocity ($\omega=2\pi N, N$ is the linear rotation speed), B is the slop of K-L plots, n is the overall number of electrons transfer, F is the Faraday constant ($F=96485~\rm C~mol^{-1}$), D_0 is the diffusion coefficient of O_2 in 0.1 M KOH ($1.9~\times~10^{-5}~\rm cm^2~s^{-1}$), v is the kinetic viscosity ($0.01~\rm cm^2~s^{-1}$), C_0 is the bulk concentration of C_0 ($1.2~\times~10^{-3}~\rm M$). Cyclic voltammetry (CV) curves were utilized to investigate the electrochemical capacitance of the catalysts. The potential range was determined in a non-Faradaic current response with a 0.1 V window cantered at open-circuit potential. CV measurements were conducted by sweeping the potential at different scan rates (20, 40, 60, 80, and $100~\rm mV~s^{-1}$). All the measured current in the CV curves is assumed to be the double-layer charging. The electrochemical double-layer capacitance, $C_{\rm cl}$, is equal to the ratio of double-layer charging current and the product of the scan rate.

2.5. Zn-air battery assembly

The homogenous ink of as-prepared catalyst or 20% Pt/C + IrO₂ for ORR and OER testing can also be used for preparing cathode of ZAB, 100 μ L of ink was dropped onto 0.38 cm² of a hydrophobic carbon cloth to achieve ~0.5 mg cm². Then the catalyst cathode was paired with a polished zinc foil, and assembled in a cointype cell with 6 M KOH and 0.25 M Zn(OAc)₂. A glass paper was paired as the separator.

3. Results and discussion

The obtained sample was first examined by XRD. As shown in Fig. S1, there is no obvious peak assigned to metal or their compounds for all the samples, indicating the metal species is amorphous or highly dispersed. The Fe content was measured to be 6.6 wt% based on the inductively coupled plasma mass spectrometry (ICP-MS). Then the morphology was characterized by SEM and TEM. As observed in SEM and TEM images (Figs. S2, S3, and Fig. 1b), the FeNxC preserves the typical graphene sheet-like morphology without observable nanoparticle or nanocluster as the morphology of pristine NC. These results are consistent with the XRD results. Additionally, the carbon lattice of resultant catalyst was investigated by Raman spectrum (Fig. S4). Both FeNxC and NC exhibit typical D band at 1340 cm⁻¹ (disordered sp³ carbon) and G band at 1580 cm $^{-1}$ (graphite sp^2 carbon). And the ratio of integrated intensity of the D and G bands (I_D/I_G) is larger than 1.1 for both FeNxC and NC, indicating large number of structural defects and disorder carbon in FeNxC and NC catalyst [11,38]. The BET analysis indicates that Fe-doping can increase the surface area (Fig. S5), thus exposing more catalytic sites and facilitating the mass- and charge transport during the catalytic reaction process.

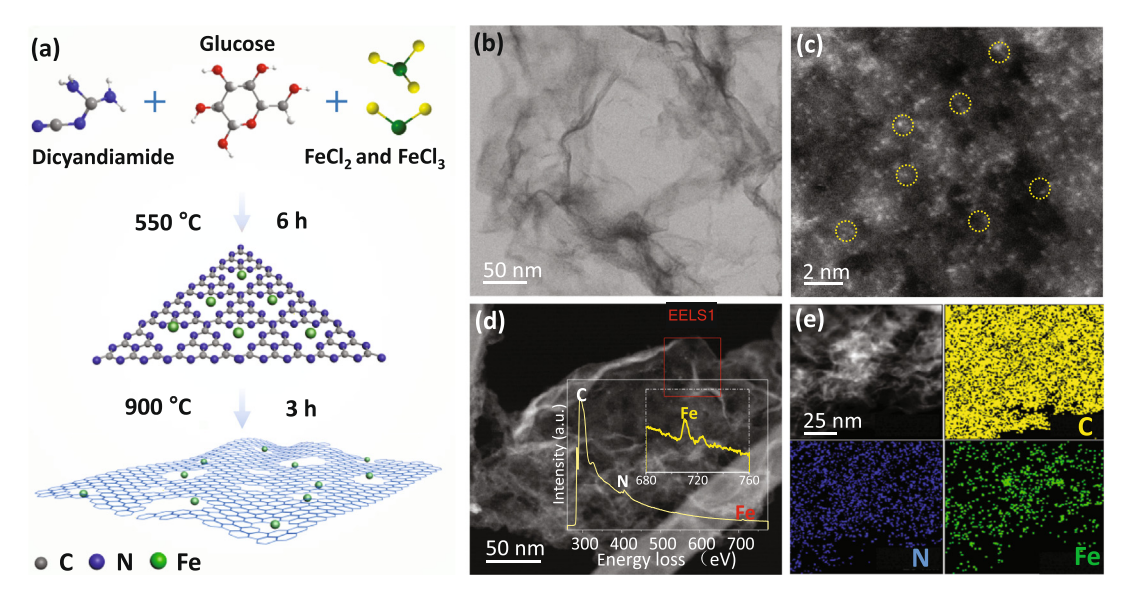


Fig. 1. Synthesis and structural characterizations. (a) Schematic illustration for synthesizing FeNx moieties in 2D carbon layer. (b) STEM image of FeNxC. (c) High-magnification HAADF-STEM image of FeNxC; the FeNx sites are bright spots highlighted by yellow circles. (d) High-magnification HAADF-STEM image of FeNxC; the inset is corresponding EELS recorded from the marked area in (d). (e) HAADF-STEM image, and corresponding EDS mapping images of FeNxC, C (yellow), N (blue) and Fe (green).

To determine the atomic structure, high-angle annular dark-field SETM (HAADF-STEM) was conducted under 80 keV. As observed in Fig. 1(c), the isolated Fe atom have the size about 0.2 nm and homogenously dispersed over the N-doped carbon layer. Furthermore, the electron energy loss spectroscopy (EELS) derived from the red square reconfirms the presence of Fe in the FeNxC catalyst (Fig. 1d). The EDS spectrum (Fig. S6) exhibits the peaks assigned to the Fe element, and related elemental mapping EDS mapping (Fig. 1e) shows the uniform dispersion of C, N and Fe.

The valence state of element was further investigated by XPS. As shown in Fig. S7, the peak of C, O, N was detected both in the NC and FeNxC catalyst. The N content is about 9.0 wt% based on XPS. And the high-resolution N 1s spectrum can be well deconvoluted into five characteristic peaks located at 404.1, 402.0, 400.5 and 398.3 eV, which are assigned to oxidized N, quaternary N, pyrrolic-N and pyridinic-N/Fe-N, respectively [39-42] (Fig. 2a). And it is obvious that FeNxC exhibits higher proportion of quaternary N and pyridinic N than that of NC due to the presence of Fe. The heteroatom dopant can modify the polarity of carbon matrix, thus improve the wettability of carbon layer, meanwhile, it can provide more active sites for ORR in FeNxC catalyst [43-49]. The high-resolution Fe 2p spectrum reveals the presence of Fe 2p1/2(723.7 and 719.7 eV) [50,51], Fe-N bonding (707.9 eV) [52-54], Fe 2p3/2 (714.2 and 710.9 eV) [55,56] (Fig. 2b). These results confirm the successful integration of discrete FeNx site into 2D carbon

And the electronic structure and coordination structure of Fe was further examined by XANES and extended X-ray absorption fine structure (EXAFS). As shown in Fig. 2(c), the absorption edge of XANES spectra of FeNxC is located between those of Fe₂O₃ and Fe foil, suggesting the Fe atom hold partially positive charges. And in the EXAFS of FeNxC, the dominant peak located at 1.5 Å, which can be ascribed to the Fe-N coordination [57]. In addition, the best fitting of the obtained EXAFS data reveals that the Fe is four-coordinated with N atom and anchored on carbon layer (Table S1). This observation is well in line with the XPS and STEM results, indicating atomically dispersed FeNx on carbon layer.

The ORR performance was evaluated via rotating ring-disk electrode (RDE) testing. The mass loading of different catalysts is about

 $0.3~\text{mg}~\text{cm}^{-2}$. The CV curves testing in O_2 - and N_2 -saturated 0.1~MKOH were recorded in Fig. 3(a), both NC and FeNxC exhibit apparent oxygen reduction peaks measured in O2-saturated electrolyte, suggesting an evident oxygen reduction process. And the peak potential of FeNxC is positively shifted about 140 mV compared with that of NC. The ORR activity of FeNxC was further investigated by LSV measurements under O₂-saturated 0.1 M KOH. As shown in Fig. 3(b), the FeNxC catalyst exhibits a half-wave potential $(E_{1/2})$ of 0.86 V, which is more positive than NC ($E_{1/2}$ = 0.73 V) and even superior to that of commercial Pt/C ($E_{1/2}$ = 0.82 V). Meanwhile, the kinetic current density of FeNxC can reach 22.1 mA cm⁻², while the Pt/C and NC just reach 10.1 and 1.3 mA cm⁻², respectively (Fig. 3c). In addition, the FeNxC exhibits the smallest tafel slop of 57.10 mV dec^{-1} compared with the NC (93.28 mV dec^{-1}), and Pt/C (73.67 mV dec⁻¹), further indicating superior kinetics of FeNxC for ORR (Fig. 3d). And the electrochemical impedance spectroscopy (EIS) was evaluated at 0.8 V vs. RHE. As shown in Fig. 3(e), FeNxC exhibits smaller semicircle than that of NC and Pt/C, which reveals fast charge transfer of FeNxC for reaction. The Koutecky-Levich (K-L) plots of FeNxC was obtained by performing LSV under different rotation speed from 400 to 2050 r min⁻¹ (Fig. S8). The electron transfer number (n) of FeNxC is about 3.70 based on the K-L equitation, indicating a 4-electron pathway during the ORR process.

The $C_{\rm dl}$ is measured to define the active surface area for NC and FeNxC catalysts. As shown in Fig. S9, the active surface area of FeNxC is 12.70 mF cm⁻², which is higher than that of NC (6.26 mF cm⁻²), indicating that FeNxC possesses more electrochemical active sites. The stability of FeNxC was evaluated by cycling the catalyst within a range of 0.6–1.1 V under a scanning rate of 100 mV s⁻¹ in O₂-saturated electrolyte. After 3000 cycles, there is almost no shift for $E_{1/2}$ for FeNxC, evidencing the superb durability of FeNxC (Fig. 3f).

Density functional theory (DFT) calculations were performed to investigate the elementary reactions of ORR over FeNxC moieties under various electrodes potential. The free energy diagram of ORR over the FeNxC is shown in Fig. 4(a). And atomic structure of involved intermediates during the reaction is shown in Fig. 4 (b). At U = 0 V, all the reaction steps are downhills, suggesting all the electron-transfer steps are exothermic. However, when at the

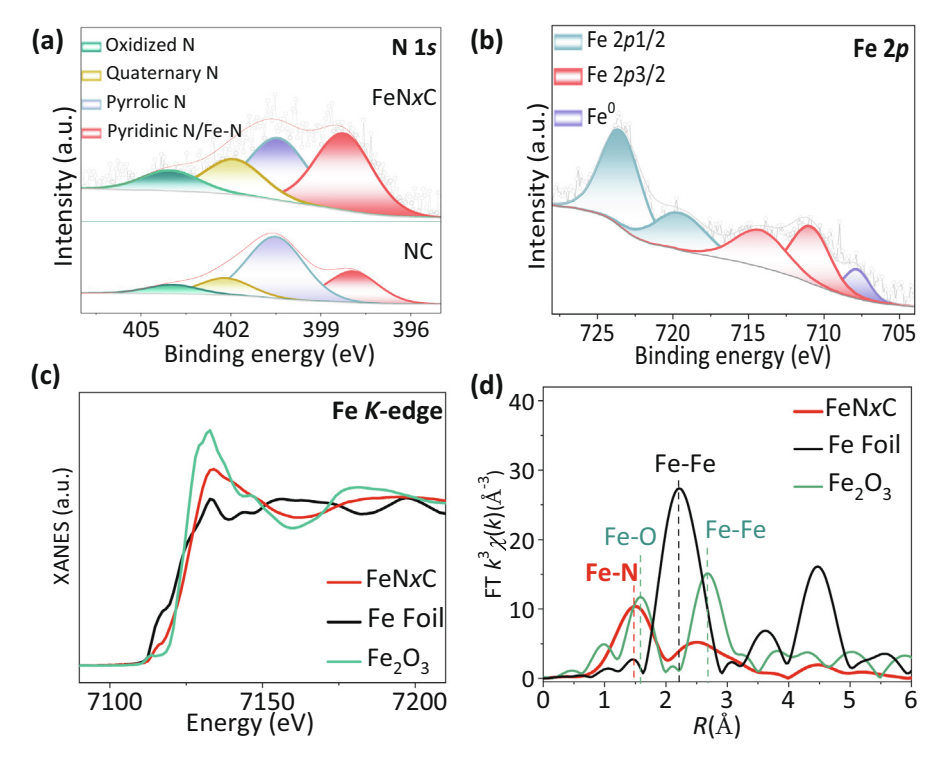


Fig. 2. Chemical states and coordination structures. XPS spectra of (a) N 1s and (b) Fe 2p in FeNxC. (c) Normalized XANES spectra at Fe K-edge of FeNxC, Fe₂O₃ and Fe foil. (d) Fourier transfer (FT) at Fe K-edge of FeNxC, Fe₂O₃ and Fe foil.

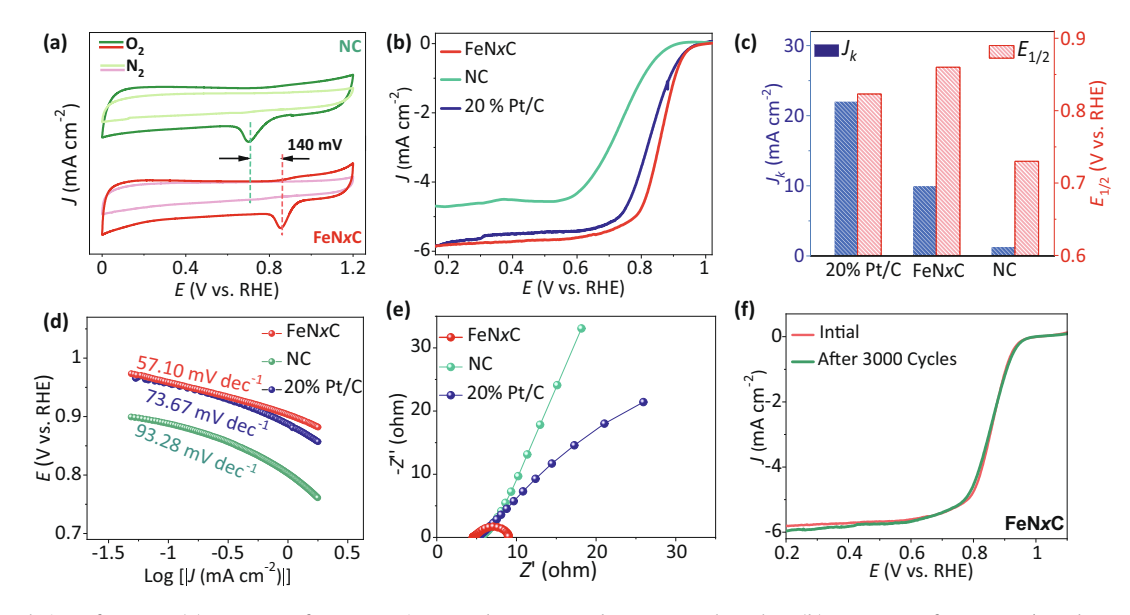


Fig. 3. Electrocatalytic performance. (a) CV curves of FeNxC test in O_2 - and N_2 - saturated 0.1 M KOH electrolyte. (b) LSV curves of NC, 20% Pt/C and FeNxC in O_2 -saturated 0.1 M KOH at the scan rate of 10 mV s⁻¹. (c) Kinetic current density and half-wave potential ($E_{1/2}$) of FeNxC, NC and Pt/C. (d) Tafel slop of FeNxC, NC and Pt/C. (e) Nyquist plots of NC, FeNxC and Pt/C. (f) Durability test of FeNxC for ORR.

equilibrium potential, U = 1.23 V, the reaction step of *OH to H_2O is uphill with the large energy barrier of 0.36 eV. Thus, the onset potential is predicted to be 0.87 V for FeNxC, which is well in good consistency with the experimental result. And the overpotential of the FeNxC is even comparable to that of noble metal catalyst [28]. The free energy change of OER pathway was also calculated as shown in Fig. S10. Under the U = 1.23 V, the conversion of O* into OOH* is the rate-determining step with a low barrier of 0.43 eV.

The potential difference of ORR potential and OER potential was investigated in O_2 -saturated 0.1 M KOH at 10 mV cm⁻². In Fig. 5(a),

FeNxC shows greater catalytic current as compared with parent NC and even surpass the state-of-the-art OER catalyst of IrO_2 due to the existence of lots of active sites on FeNxC. Obviously, the overall oxygen performance of FeNxC suppress that of NC ($\Delta E = 1.02$ V) and Pt/C + IrO_2 ($\Delta E = 0.99$ V), which exhibits the smallest overpotential of 0.94 V. This excellent result also surpasses the similar Febased single atom bifunctional catalyst reported [34,37]. Encouraged by the excellent bifunctional ORR and OER performance of FeNxC, a coin-type Zn-air battery was assembled using the FeNxC as the cathode to further evaluate the electrochemical performance

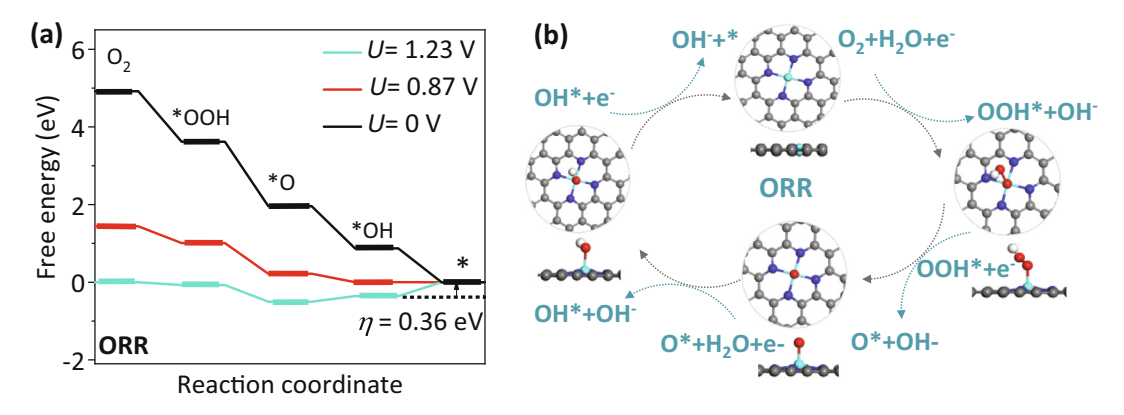


Fig. 4. (a) Free energy profile of the ORR for the FeNxC. (b) The atomic structure of the FeNxC model as determined by DFT calculations. The cyan, blue, grey, red and white spheres depict Fe, N, C, O and H, respectively.

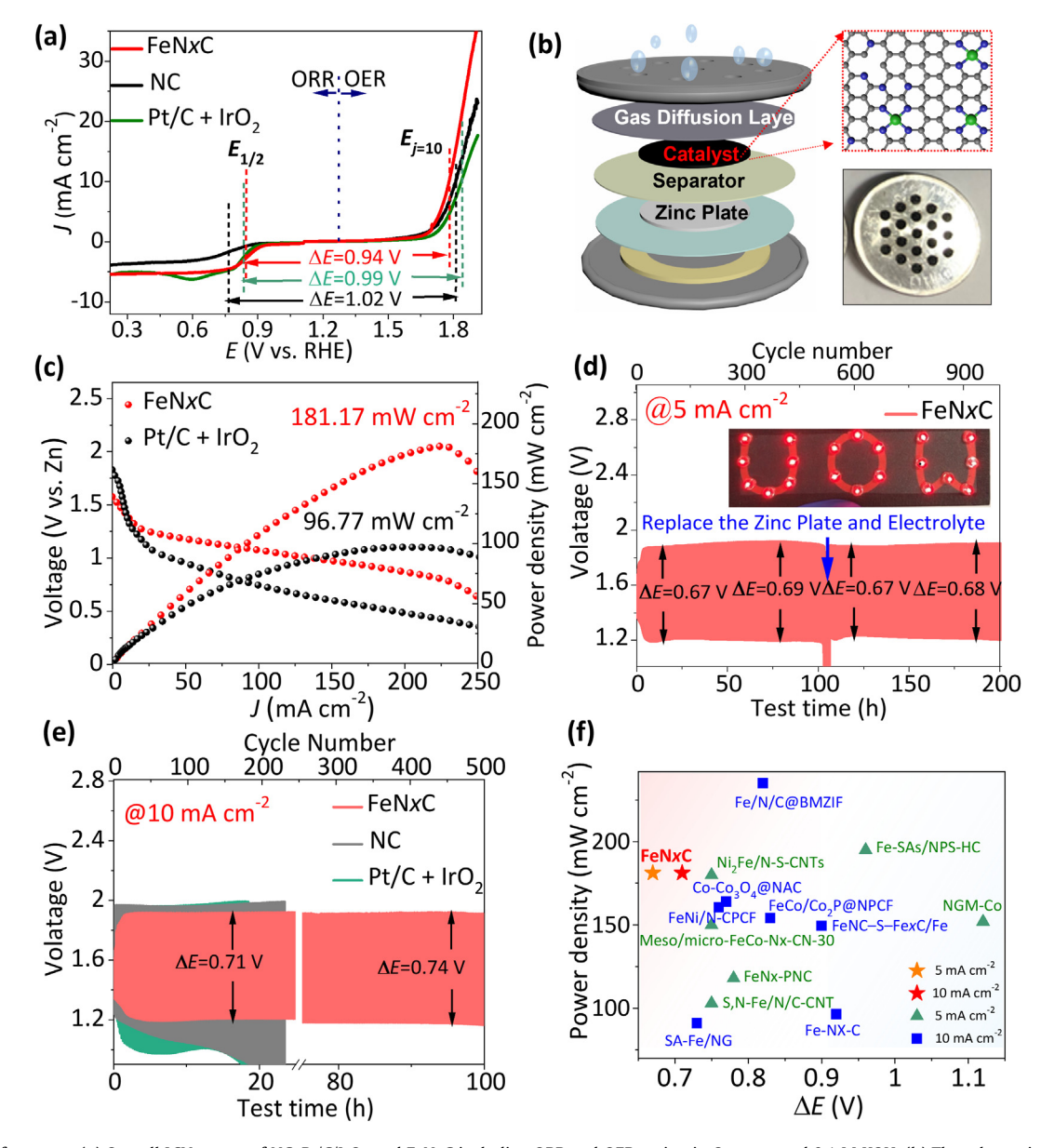


Fig. 5. ZAB performance. (a) Overall LSV curves of NC, $Pt/C/IrO_2$ and FeNxC including ORR and OER region in O_2 -saturated 0.1 M KOH. (b) The schematic illustration of the coin-type Zn-air battery (right top inset is atomic structure of FeNxC, and right bottom inset is the photography of coin-type ZAB). (c) Galvanostatic discharge and corresponding power density plots. (d) Galvanostatic discharge-charge cycling performance at the current density of 5 mA cm⁻². Inset shows the lighted LED screen powered by four Zn-air batteries in series. (e) Cycling performance of NC, $Pt/C + IrO_2$ and FeNxC as air cathode under the current density of 10 mA cm⁻². (f) Comparison of power density and voltage gap for various single atom-based catalysts. Values were plotted from references (Table S1).

in real application. As illustrated in Fig. 5(b), the ZAB is packaged in coin-type cell using 6 M KOH and 0.25 M zinc acetate as electrolyte, and FeNxC-loaded carbon cloth and a zinc plate (0.5 mg cm^{-2}) as the air cathode and anode, respectively. And the hydrophobic carbon cloth (Cetech, W1S1009) can serve as the gas diffusion layer to ensure that O2 can freely flow inside the electrode and prevent evaporation of the electrolyte. The EIS spectrum shows the batteries with various catalysts have similar internal resistance of $\sim 2 \Omega$, suggesting the operating condition is similar (Fig. S12). Fig. S13 shows that the FeNxC-based output high open-circuit voltage of 1.41 V, which is higher than that of Pt/ C + IrO₂ and NC. In addition, in comparison with Pt/C + IrO₂based battery, the charging-discharging polarization curves for FeNxC-based battery exhibits a shrunken voltage gap (Fig. S14). Also, the maximum power density of FeNxC-based ZAB is 181.2 mW cm⁻² (Fig. 5c), which is almost 2-fold greater than that of Pt/C + IrO_2 -based ZAB (96.8 mW cm⁻²).

The battery cycling stability of FeNxC-equipped ZAB is further tested under the current density of 5 mA cm⁻². Moreover, when the zinc plate and electrolyte was replenished after 100 h, the ZAB still can be regenerated without performance degradation, and the average voltage gap between charge and discharge is 0.67 V. Furthermore, it exhibits an ultra-long battery lifetime close to 200 h and 1000 cycles, indicating good battery durability. And four Zn-air batteries connected in series can light the red light emitting diodes (LEDs) screen (Fig. 5d). The battery cyclic stability and rate capability of FeNxC are further tested at the current density of 10 mA cm⁻² (10 min for each cycle). Impressively, the average charge-discharge voltage gap ($\Delta E = 0.71 \text{ V}$) at higher current density just exhibits slight increase of ~ 6% than that under 5 mA cm⁻² (ΔE = 0.67 V), indicating the good rate capability (Fig. 5e). Even after 500 cycles, the voltage gap just has a slight drop of 0.03 V, suggesting good stability and reversibility when using FeNxC as the air cathode. In contrast, the NC-based and Pt/ C + IrO₂-based ZAB exhibit larger voltage gap and inferior stability. Moreover, the power density and voltage gap of the FeNxC is superior to most of the reported SACs-based catalysts (Fig. 5f). As shown in Fig. S15, the ZAB with FeNxC exhibits a discharge voltage of about 1.25 V and remains 10.9 h at the discharging current of 20 mA cm $^{-2}$, similar with that of Pt/C + IrO₂ (1.23 V, 10.9 h). Moreover, the all-solid-state ZABs were prepared by using a solid alkaline polyvinyl alcohol (PVA) polymer electrolyte as the separator. The all-solid-state ZAB of FeNxC can run stably for more than 3000 s at 1 mA cm⁻², and the voltage gap between discharging and charging is about 0.7 V (Fig. S16). XRD, XPS and TEM measurements were performed after the stability measurements (see Fig. S17). There are no noticeable changes in the structural, morphological and compositional properties of FeNxC, suggesting that electrocatalyst is stable in alkaline KOH solutions. These results together suggest that FeNxC possesses an appreciable intrinsic ORR activity as well as good Zn-air battery performance.

4. Conclusions

In summary, a one-pot pyrolysis strategy was developed to synthesize the atomically dispersed FeNxC for efficient ORR catalyst. The ORR performance of FeNxC is experimentally and theoretically demonstrated. The resultant FeNxC catalyst exhibits remarkable ORR performance with half-wave potential of 0.86 V along with good stability. The Zn-air battery assembled with FeNxC evidence impressive performance, which can deliver maximum power density with 181.2 mW cm⁻² and a low voltage gap of 0.71 V even at 10.0 mA cm⁻². Our work not only offers a versatile strategy to synthesize highly efficient single atom-based catalyst, but also provides a major boost for highly efficient and durable ZABs.

Declaration of Competing Interest

The authors declare that they have no known competing financial interests or personal relationships that could have appeared to influence the work reported in this paper.

Acknowledgments

This research was financially supported by the Shenzhen Science and Technology Research Grant (JCYJ20200109140416788), the Chemistry and Chemical Engineering Guangdong Laboratory (1922018), and the National Key R&D Program of China (2020YFB0704500). The authors also would like to acknowledge the financial support from the China Scholarship Council (CSC) and the Australian Research Council (ARC) through an ARC project (ARC DP160102627 and ARC DP170101467), and acknowledge the use of facilities within the UOW Electron Microscopy Centre, with particular thanks to Dr. Gilberto Casillas-Carcia.

Appendix A. Supplementary data

Supplementary data to this article can be found online at https://doi.org/10.1016/j.jechem.2021.07.009.

References

- [1] Y. Li, H. Dai, Chem. Soc. Rev. 43 (2014) 5257-5275.
- [2] B.J. Hopkins, Y. Shao-Horn, D.P. Hart, Science 362 (2018) 658–661.
- [3] J. Fu, Z.P. Cano, M.G. Park, A. Yu, M. Fowler, Z. Chen, Adv. Mater. 29 (2017) 1604685.
- [4] W. Sun, F. Wang, B. Zhang, M. Zhang, V. Küpers, X. Ji, C. Theile, P. Bieker, K. Xu, C. Wang, Science 371 (2021) 46–51.
- [5] B.Q. Li, C.X. Zhao, S. Chen, J.N. Liu, X. Chen, L. Song, Q. Zhang, Adv. Mater. 31 (2019) 1900592.
- [6] C. Mu, J. Mao, J. Guo, Q. Guo, Z. Li, W. Qin, Z. Hu, K. Davey, T. Ling, S.Z. Qiao, Adv. Mater. 32 (2020) 1907168.
- [7] D. Jiao, Z. Ma, J. Li, Y. Han, J. Mao, T. Ling, S. Qiao, J. Energy Chem. 44 (2020) 1–7.
- [8] Y. Jiao, Y. Zheng, M. Jaroniec, S.Z. Qiao, Chem. Soc. Rev. 44 (2015) 2060-2086.
- [9] H. Wu, H. Li, X. Zhao, Q. Liu, J. Wang, J. Xiao, S. Xie, R. Si, F. Yang, S. Miao, Energy Environ. Sci. 9 (2016) 3736–3745.
- [10] Y.J. Li, L. Cui, P.F. Da, K.W. Qiu, W.J. Qin, W.B. Hu, X.W. Du, K. Davey, T. Ling, S.Z. Qiao, Adv. Mater. 30 (2018) 1804653.
- [11] H.B. Yang, J. Miao, S.-F. Hung, J. Chen, H.B. Tao, X. Wang, L. Zhang, R. Chen, J. Gao, H.M. Chen, Sci. Adv. 2 (2016) e1501122.
- [12] L. Liu, A. Corma, Chem. Rev. 118 (2018) 4981-5079.
- [13] H. Xu, D. Cheng, D. Cao, X.C. Zeng, Nat. Catal. 1 (2018) 339–348.
- [14] W.H. Lai, L.F. Zhang, W.B. Hua, S. Indris, Z.C. Yan, Z. Hu, B. Zhang, Y. Liu, L. Wang, M. Liu, Angew. Chem. Int. Ed. 131 (2019) (1999) 11994–12001.
- [15] Y. Chen, S. Ji, C. Chen, Q. Peng, D. Wang, Y. Li, Joule 2 (2018) 1242-1264.
- [16] B. Qiao, A. Wang, X. Yang, L.F. Allard, Z. Jiang, Y. Cui, J. Liu, J. Li, T. Zhang, Nat. Chem. 3 (2011) 634–641.
- [17] H. Fei, J. Dong, Y. Feng, C.S. Allen, C. Wan, B. Volosskiy, M. Li, Z. Zhao, Y. Wang, H. Sun, Nat. Catal. 1 (2018) 63–72.
- [18] Z. Yang, Y. Wang, M. Zhu, Z. Li, W. Chen, W. Wei, T. Yuan, Y. Qu, Q. Xu, C. Zhao, ACS Catal. 9 (2019) 2158–2163.
- [19] L. Yang, D. Cheng, H. Xu, X. Zeng, X. Wan, J. Shui, Z. Xiang, D. Cao, Natl. Acad. Sci. USA 115 (2018) 6626–6631.
- [20] Y. Chen, S. Ji, S. Zhao, W. Chen, J. Dong, W.-C. Cheong, R. Shen, X. Wen, L. Zheng, A.I. Rykov, Nat. Commun. 9 (2018) 1–12.
- [21] R. Wang, Y. Yang, Y. Zhao, L. Yang, P. Yin, J. Mao, T. Ling, J. Energy Chem. 58 (2021) 629–635.
- [22] F. Li, G.-F. Han, H.-J. Noh, S.-J. Kim, Y. Lu, H.Y. Jeong, Z. Fu, J.-B. Baek, Energy Environ. Sci. 11 (2018) 2263–2269.
- [23] W. Zang, A. Sumboja, Y. Ma, H. Zhang, Y. Wu, S. Wu, H. Wu, Z. Liu, C. Guan, J. Wang, ACS Catal. 8 (2018) 8961–8969.
- [24] P. Yin, T. Yao, Y. Wu, L. Zheng, Y. Lin, W. Liu, H. Ju, J. Zhu, X. Hong, Z. Deng, Angew. Chem. Int. Ed. 128 (2016) 10958–10963.
- [25] J. Li, S. Chen, N. Yang, M. Deng, S. Ibraheem, J. Deng, J. Li, L. Li, Z. Wei, Angew. Chem. Int. Ed. 58 (2019) 7035–7039.
- [26] E. Luo, H. Zhang, X. Wang, L. Gao, L. Gong, T. Zhao, Z. Jin, J. Ge, Z. Jiang, C. Liu, Angew. Chem. Int. Ed. 58 (2019) 12469–12475.
- [27] C. Zhang, J. Sha, H. Fei, M. Liu, S. Yazdi, J. Zhang, Q. Zhong, X. Zou, N. Zhao, H. Yu, ACS Nano 11 (2017) 6930–6941.
- [28] M. Xiao, J. Zhu, G. Li, N. Li, S. Li, Z.P. Cano, L. Ma, P. Cui, P. Xu, G. Jiang, Angew. Chem. Int. Ed. 131 (2019) 9742–9747.
- [29] A. Zitolo, V. Goellner, V. Armel, M.-T. Sougrati, T. Mineva, L. Stievano, E. Fonda, F. Jaouen, Nat. Mater. 14 (2015) 937–942.

- [30] Y. Wang, H. Yuan, Y. Li, Z. Chen, Nanoscale 7 (2015) 11633-11641.
- [31] L. Jiao, G. Wan, R. Zhang, H. Zhou, S.H. Yu, H.L. Jiang, Angew. Chem. Int. Ed. 57 (2018) 8525–8529.
- [32] W.-J. Jiang, L. Gu, L. Li, Y. Zhang, X. Zhang, L.-J. Zhang, J.-Q. Wang, J.-S. Hu, Z. Wei, L.-J. Wan, J. Am. Chem. Soc. 138 (2016) 3570–3578.
- [33] A. Kulkarni, S. Siahrostami, A. Patel, J.K. Nørskov, Chem. Rev. 118 (2018) 2302– 2312.
- [34] J. Han, X. Meng, L. Lu, J. Bian, Z. Li, C. Sun, Adv. Funct. Mater. 29 (2019) 1808872.
- [35] Y. Qiao, P. Yuan, Y. Hu, J. Zhang, S. Mu, J. Zhou, H. Li, H. Xia, J. He, Q. Xu, Adv. Mater. 30 (2018) 1804504.
- [36] Y.J. Sa, D.-J. Seo, J. Woo, J.T. Lim, J.Y. Cheon, S.Y. Yang, J.M. Lee, D. Kang, T.J. Shin, H.S. Shin, J. Am. Chem. Soc. 138 (2016) 15046–15056.
- [37] L. Ma, S. Chen, Z. Pei, Y. Huang, G. Liang, F. Mo, Q. Yang, J. Su, Y. Gao, J.A. Zapien, ACS Nano 12 (2018) 1949–1958.
- [38] I.Y. Jeon, S. Zhang, L. Zhang, H.J. Choi, J.M. Seo, Z. Xia, L. Dai, J.B. Baek, Adv. Mater. 25 (2013) 6138–6145.
- [39] N. Wang, W. Ma, Z. Ren, Y. Du, P. Xu, X. Han, J. Mater. Chem. A 6 (2018) 884–895.
- [40] N. Hellgren, R.T. Haasch, S. Schmidt, L. Hultman, I. Petrov, Carbon 108 (2016) 242–252.
- [41] D. Zhao, K. Sun, W.C. Cheong, L. Zheng, C. Zhang, S. Liu, X. Cao, K. Wu, Y. Pan, Z. Zhuang, Angew. Chem. Int. Ed. 132 (2020) 9067–9075.
- [42] Y. Sun, Z. Zhang, Y. Sun, G. Yang, Int. J. Agric. Biol. Eng. 13 (2020) 207-214.
- [43] Z. Wang, J. Ang, J. Liu, X.Y.D. Ma, J. Kong, Y. Zhang, T. Yan, X. Lu, Appl. Catal. B: Environ. 263 (2020) 118344.

- [44] C.Y. Su, H. Cheng, W. Li, Z.Q. Liu, N. Li, Z. Hou, F.Q. Bai, H.X. Zhang, T.Y. Ma, Adv. Energy Mater. 7 (2017) 1602420.
- [45] L. Miao, D. Zhu, M. Liu, H. Duan, Z. Wang, Y. Lv, W. Xiong, Q. Zhu, L. Li, X. Chai, Chem. Eng. J. 347 (2018) 233–242.
- [46] D. Guo, R. Shibuya, C. Akiba, S. Saji, T. Kondo, J. Nakamura, Science 351 (2016) 361–365.
- [47] D. Zhang, L. Zheng, Y. Ma, L. Lei, Q. Li, Y. Li, H. Luo, H. Feng, Y. Hao, ACS Appl. Mater. Interfaces 6 (2014) 2657–2665.
- [48] K. Gong, F. Du, Z. Xia, M. Durstock, L. Dai, Science 323 (2009) 760-764.
- [49] G. Liu, X. Li, P. Ganesan, B.N. Popov, Appl. Catal. B: Environ. 93 (2009) 156–165.
- [50] W. Li, B. Yu, Y. Hu, X. Wang, B. Wang, X. Zhang, D. Yang, Z. Wang, Y. Chen, J. Power Sources 456 (2020) 228015.
- [51] J.-Y. Xie, Z.-Z. Liu, J. Li, L. Feng, M. Yang, Y. Ma, D.-P. Liu, L. Wang, Y.-M. Chai, B. Dong, J. Energy Chem. 48 (2020) 328–333.
- [52] Y. Zhao, J. Zhang, X. Guo, H. Fan, W. Wu, H. Liu, G. Wang, J. Mater. Chem. A 5 (2017) 19672–19679.
- [53] H. Zhang, Q. Gong, S. Ren, M.A. Arshid, W. Chu, C. Chen, Catal. Sci. Technol. 8 (2018) 907–915.
- [54] C. Wang, Q. Yang, Z. Li, K.-Y.-A. Lin, S. Tong, Sep. Purif. Technol. 213 (2019) 447–455.
- [55] X. Cao, Y. Chen, S. Jiao, Z. Fang, M. Xu, X. Liu, L. Li, G. Pang, S. Feng, Nanoscale 6 (2014) 12366–12370.
- [56] Z. Zhou, F. He, Y. Shen, X. Chen, Y. Yang, S. Liu, T. Mori, Y. Zhang, Chem. Commun. 53 (2017) 2044–2047.
- [57] M. Yan, Z. Dai, S. Chen, L. Dong, X.L. Zhang, Y. Xu, C. Sun, J. Phys. Chem. C 124 (2020) 13283–13290.